The Astrophysical Journal, 929:179 (11pp), 2022 April 20 https://doi.org/10.3847/1538-4357/ac6176

Detection of a Prompt Fast-variable Thermal Component in the Multipulse Short Gamma-Ray Burst 170206A

Peng-Wei Zhao[1], Qing-Wen Tang[1], Yuan-Chuan Zou[2], and Kai Wang[2]
[1] Department of Physics, School of Physics and Materials Science, Nanchang University, Nanchang 330031, People's Republic of China; qwtang@ncu.edu.cn
[2] School of Physics, Huazhong University of Science and Technology, Wuhan 430074, People's Republic of China; zouyc@hust.edu.cn, kaiwang@hust.edu.cn
Received 2021 December 29; revised 2022 March 24; accepted 2022 March 24; published 2022 April 27

Abstract

We report the detection of a strong thermal component in the short gamma-ray burst 170206A with three intense pulses in its light curves, throughout which the fluxes of this thermal component exhibit fast temporal variability the same as that of the accompanying nonthermal component. The values of the time-resolved low-energy photon index in the nonthermal component are between about -0.79 and -0.16, most of which are harder than the $-2/3$ expected in the synchrotron emission process. In addition, we found a common evolution between the thermal component and the nonthermal component, $E_{\rm p,CPL} \propto kT_{\rm BB}^{0.95\pm0.28}$ and $F_{\rm CPL} \propto F_{\rm BB}^{0.67\pm0.18}$, where $E_{\rm p,CPL}$ and $F_{\rm CPL}$ are the peak photon energy and corresponding flux of the nonthermal component, and $kT_{\rm BB}$ and $F_{\rm BB}$ are the temperature and corresponding flux of the thermal component, respectively. Finally, we proposed that the photospheric thermal emission and the Comptonization of thermal photons may be responsible for the observational features of GRB 170206A.

Unified Astronomy Thesaurus concepts: Gamma-ray bursts (629); Astronomy data analysis (1858)

1. Introduction

Gamma-ray bursts (GRBs) are believed to arise from the deaths of massive stars or the coalescence of two compact stellar objects such as neutron stars or black holes, which are both followed by an expanding fireball with a jet. Many GRBs observed by several missions suggest the prompt gamma-ray emission to be highly nonthermal (Mazets et al. 1981; Fenimore et al. 1982; Matz et al. 1985; Kaneko et al. 2006; Goldstein et al. 2012) and generated by synchrotron radiation of accelerated electrons in intense magnetic fields (Katz 1994; Rees & Meszaros 1994; Sari et al. 1996; Tavani 1996; Sari et al. 1998). The values of the low-energy photon spectral index (α), which is harder than the $-2/3$ from the observed GRB spectra, are different from the theoretical predictions. This low-energy photon index is expected to be $-3/2$ when the electrons undergo a fast-cooling synchrotron, while it is about $-2/3$ when the electron spectrum follows a slow-cooling synchrotron emission (Sari et al. 1998). A few theoretical models have been proposed to reconcile the observed GRB prompt spectra with the synchrotron process. Some of them invoke effects that produce a hardening of the low-energy spectral index, such as a decaying magnetic field (Pe'er & Zhang 2006; Uhm & Zhang 2014; Zhang 2020; Wang & Dai 2021), inverse Compton scattering in the Klein–Nishina regime, or a marginally fast cooling regime (Derishev et al. 2001; Nakar et al. 2009; Wang et al. 2009; Daigne et al. 2011).

Actually, the emission from this fireball is expected to be thermal, which originated from the nondissipative photosphere (Goodman 1986; Paczynski 1986; Rees & Meszaros 1994; Ryde 2004; Pe'er 2008; Beloborodov 2010, 2011; Pe'er & Ryde 2011; Ghirlanda et al. 2013; Larsson et al. 2015; Ryde et al. 2017). This pure thermal component fitted by a standard Planck blackbody function (hereafter BB) is found in many Fermi Gamma-Ray Burst Monitor (GBM) GRBs, such as GRB 150101B and other GRBs (Burns et al. 2018; Acuner et al. 2019, 2020). Even the low-energy photon index is acceptable in the synchrotron theory; modified thermal processes have been proposed to account for the observations, such as a dissipative photosphere (Rees & Mészáros 2005; Giannios 2012; Veres et al. 2012; Lundman et al. 2013, 2014, 2018). A trend has therefore evolved with the possibility of reconciling synchrotron emission with the α distributions, which consists of fitting a BB (nondissipative photosphere) in combination with the typically fitted nonthermal spectral function to spectra observed by Fermi-GBM (Ryde 2005; Battelino et al. 2007; Guiriec et al. 2011; Axelsson et al. 2012; Guiriec et al. 2013; Iyyani et al. 2013; Preece et al. 2014; Burgess et al. 2015; Zou et al. 2015; Tang et al. 2021).

GRB 120323A was the first short GRB (SGRB) with contemporaneous detection of the thermal component and nonthermal component in the prompt phase, with single-pulse lightcurves and a decaying pattern both in its thermal flux and thermal temperature (Guiriec et al. 2013). Among the top 10 brightest fluence-selected SGRBs detected by Fermi-GBM as of 2021 December, we have searched for such spectral properties and found GRB 170206A with a strong thermal-component detection, which however shows very different properties from GRB 120303A, such as the tracking pattern between the thermal component and nonthermal component. In this work, we report the results of this unique SGRB and explore its possible physical origins. This paper is organized as follows. In Section 2, we present the observations of GRB 170206A. In Section 3, data analysis of GRB 170206A and the results are presented. In Section 4, we discuss the origins of these two spectral components. The conclusion and discussion are presented in Section 5.

2. Observations

GRB 170206A triggered the Fermi-GBM at 10:51:57.70 UT on 2017 February 6 (T_0) with R.A.$_{\rm GBM}=211.^{\circ}80$, decl.$_{\rm GBM}=13.^{\circ}06$ and 1σ uncertainty of $1.^{\circ}14$. The GBM light curve shows a short, bright burst with a duration of about 1.2 s in the energy range of 50–300 keV (von Kienlin & Roberts 2017). It was also detected by the Fermi Large Area Telescope (LAT) with the best location at R.A.$_{\rm LAT}=212.^{\circ}79$, decl.$_{\rm LAT}=14.^{\circ}48$ and the 90% containment statistical error radius $0.^{\circ}85$, which is consistent with the GBM position. The angle from the Fermi/LAT boresight at the GBM trigger time (T_0) is about 67°; the highest-energy photon detected by LAT is about 811 MeV event, which is observed 3.17 s after the GBM trigger (Dirirsa et al. 2017).

GRB 170206A was detected by Konus-Wind, INTEGRAL/SPI-ACS, and Mars-Odyssey/HEND, with its center located at R.A.$_{\rm IPN}=212.^{\circ}63$ and decl.$_{\rm IPN}=14.^{\circ}24$ (Hurley et al. 2017; Svinkin et al. 2017). POLAR on board the Chinese space laboratory Tiangong-2 detected it in the energy range of about 20–500 keV, which shows that GRB 170206A consists of multiple peaks, with the minimum detectable polarization of about 5.7% (Wang et al. 2017).

3. Data Analysis

3.1. Event Selections

For the GBM data, three NaI detectors closest to the GRB position (*n*9, *na*, and *nb*) and one BGO detector (*b*1) with the lowest angle of incidence are included. For the time-tagged event (TTE) from these NaI detectors employed in the following sections, we ignore the last two channels and events with photon energy less than 8 keV. For TTE data of the BGO detector, the channels with energy below 200 keV and above 40 MeV are ignored. We choose the time intervals of [−25 s, −10 s] and [15 s, 30 s] away from the GBM trigger time to fit the background. Instrument response files are selected with the *rsp2* files throughout the data analysis.

For the LAT data, the LAT–*Transient020E* events with a zenith angle cut of 100° are selected, the energy of which are between 100 MeV and 10 GeV. The region of interest (ROI) is chosen within the radius of 12° from the Fermi/LAT localization, such as R.A.$_{\rm LAT}=212.^{\circ}79$, decl.$_{\rm LAT}=14.^{\circ}48$.

3.2. Temporal Analysis

We built the multiwavelength GBM light curves as well as the LAT light curves, which are shown in Figure 1.

For the GBM light curves, we plotted them in three energy bands, the low-energy band (8–50 keV, hereafter the LE band); the energy band employed to estimate the GBM T_{90} (50–300 keV, hereafter the T_{90} band), among which 90% of the burst's fluence was accumulated; and the main energy range of the BGO detector (300 keV–20 MeV, hereafter the BGO band). For those light curves in the LE band and T_{90} band, the average count rates of three NaI detectors (*n*9, *na*, and *nb*) are calculated. As seen in Figure 1, light curves in both the T_{90} band and BGO band show a fast-variable property with three intensive pulses, while lightcurves in the LE band can be also distinguished by three pulses. In order to perform the time-resolved spectral analysis in the following sections, six epochs are finally derived by rebinning the TTE data of the brightest NaI detector (*n*9) using the Bayesian Blocks method (BBlocks; Scargle et al. 2013) with a false-alarm probability of $p_0=0.001$, which is the chance probability of the correct bin configuration. The derived time-resolved epochs are plotted with the red dashed vertical lines and labeled from epoch a to epoch f, among which epochs b, c, and e are dominated by the first pulse (P1), the second pulse (P2), and the third pulse (P3) as seen in Figure 1.

In order to discuss the spectral properties before and after the GBM T_{90} period (epochs a, b, c, d, e, and f), we perform the same BBlocks analysis as above in the time intervals [–0.500 s, 0.208 s], [1.376 s, 2.000 s] relative to T_0. As a result, we derived two periods nearest T_{90}, such as the Pre-T_{90} period of [T_0–0.133, T_0+0.208] and the Post-T_{90} period of [T_0+1.376, T_0+1.497], which are also employed to perform the time-integrated spectral analysis in the following sections.

As for the LAT data, we perform the unbinned likelihood analysis in the time range of 1 s before and 100 s after the GBM trigger time, and calculate the probability of each photon being associated with GRB 170206A using Fermi Science Tools (*gtsrcprob*). As seen in Table 1, there are six high-energy photon events detected by Fermi/LAT; however, only one photon within GBM T_{90} has a probability of less than 50%, thus we did not include the LAT data in the following spectral analysis (Ackermann et al. 2013; Dirirsa et al. 2017; Ajello et al. 2019).

3.3. Spectral Analysis

3.3.1. General Method

Four models are defined to fit the gamma-ray data of GRB 170206A, namely, the cutoff power-law model (CPL), the Band model (BAND), the CPL+BB model, and the BAND +BB model. For the latter two BB-joint models, the CPL+BB model consists of the CPL component and the BB component while the BAND+BB model comprises the BAND component and the BB component. These models are expressed below:

(i) The BAND model, written in the same way as that in Band et al. (1993),

$$N(E)_{\rm BAND}=A_{\rm BAND}\times\begin{cases}\left(\frac{E}{100\ {\rm keV}}\right)^{\alpha}e^{[-E(2+\alpha)/E_p]}, & E\leqslant\frac{\alpha-\beta}{2+\alpha}E_p\\ \left(\frac{(\alpha-\beta)E_p}{(2+\alpha)100\ {\rm keV}}\right)^{(\alpha-\beta)}e^{(\beta-\alpha)}\left(\frac{E}{100\ {\rm keV}}\right)^{\beta}, & E\geqslant\frac{\alpha-\beta}{2+\alpha}E_p\end{cases}, \quad (1)$$

where α and β are the low-energy photon index and the high-energy photon index, respectively, and $E_{\rm p}$ (or $E_{\rm p,\ BAND}$) is the peak energy in the νF_ν spectrum.

(ii) The CPL model is written as

$$N(E)_{\rm CPL}=A_{\rm CPL}\left(\frac{E}{100\ {\rm keV}}\right)^{\alpha}e^{-E/E_{\rm c}}, \quad (2)$$

where α is the photon index and $E_{\rm c}$ is the cutoff energy. The peak energy of the CPL model ($E_{\rm p,\ CPL}$) is calculated by $E_{\rm p,\ CPL}=(2+\alpha)\times E_{\rm c}$.

(iii) The BB model is given by

$$N(E)_{\rm BB}=A_{\rm BB}\frac{E^2}{\exp(E/kT_{\rm BB})-1}, \quad (3)$$

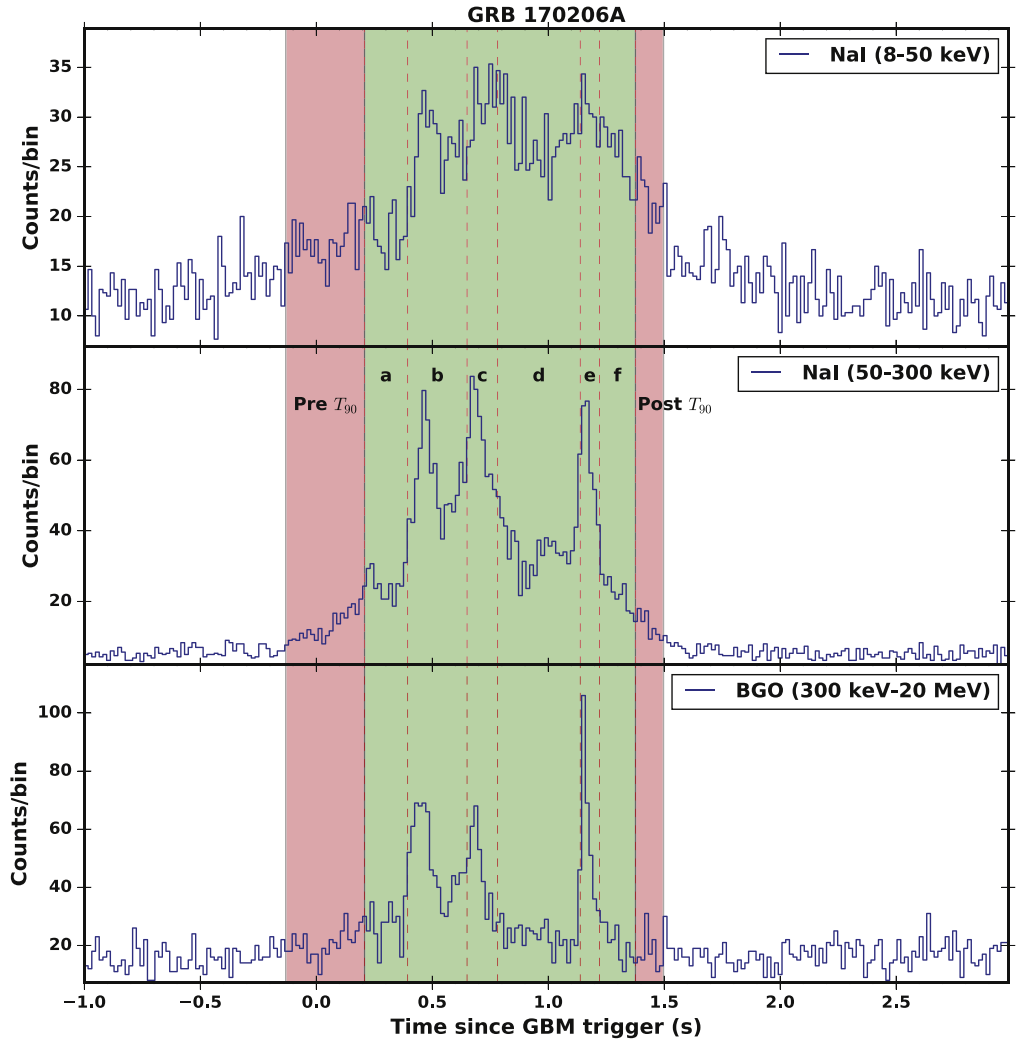

Figure 1. Composite light curves for GRB 170206A. From top to bottom, the low-energy band lightcurve (8–50 keV, LE band), GBM T_{90} band lightcurve (50–300 keV, T_{90} band), the main BGO energy band lightcurve (BGO band), and the LAT lightcurve (100 MeV–10 GeV, LAT band). The green shadowed region covers the GBM T_{90} period, the red shadows before and after which are the Pre-T_{90} period and Post-T_{90} period. respectively; for details please see the text in Section 3.2. The red dashed vertical lines divide the GBM T_{90} into six time-resolved epochs, which are labeled a to f.

Table 1
Properties of the High-energy Photons of GRB 170206A Detected by Fermi-LAT

Arrival Time[a] s	Photon Energy MeV	Probability[b]
0.85	121.7	36.97%
3.17	810.6	99.99%
6.60	389.0	96.27%
61.33	306.3	65.62%
82.51	105.9	5.55%
98.25	121.5	18.97%

Notes.
[a] Arrival time of each high-energy photon after GBM T_0.
[b] Probability of each high-energy photon associated with GRB 170206A.

where k is the Boltzmann's constant, and the joint parameter $kT_{\rm BB}$ is an output parameter in common. For all the above models, A is the amplitude. The free parameters in a candidate model are initialized at the typical spectral parameter values from the Fermi-GBM catalog (von Kienlin et al. 2020) and allowed in the broad ranges.

Six other models are also included to make comparisons, such as the main models (BAND, CPL) with an additional power-law decay model (PL) or the multicolor blackbody (mBB), which are presented in Appendix Appendix. As discussed in Appendix Appendix, the most possible model, mBB, does not fit the SED well in the T_{90} period and three time-resolved spectra, such as epochs b, d, and e, thus we did not present it in the following sections.

As a common method in GBM spectral analysis, we employ the maximum-likelihood estimate method, which is suitable for the Poisson data and the Gaussian background ($\rm PG_{stat}$; Cash 1979). For each fitting, a likelihood value $L(\vec{\theta})$ as the function of the free parameters $\vec{\theta}$ is derived, then the value of the Akaike information criterion (AIC; Akaike 1974), defined as AIC $= -2\ln L(\vec{\theta})+2k$, and the value of the Bayesian information criterion (BIC; Schwarz 1978), defined as BIC $= -2\ln L(\vec{\theta})+m\ln n$, are calculated, where m is the number of free parameters to be estimated and n is the number of observations (the sum of the selected GBM energy channels). In this work, the Multi-Mission Maximum Likelihood package (3ML;

Vianello et al. 2015) is employed to carry out all the spectral analysis and the parameter estimation.

In this paper, given any two estimated models, the preferred model is the one that provides the minimum BIC score. We use ΔBIC to describe the evidence against a candidate model as the best model in the spectral analysis of GRB 170206A. With respect to the best model with the minimum BIC ($BIC_{minimum}$), the evidence that the best model is against the candidate model is very strong when ΔBIC ($=BIC_{candidate} - BIC_{minimum}$) > 10 while ΔBIC > 6 is strong (Kass & Raftery 1995). Finally, if ΔBIC is smaller than 6, the candidate model is classified as the compared model.

3.3.2. Time-integrated Spectral Analysis

We perform the time-integrated spectral analysis of GRB 170206A in three main time intervals, that is, the Pre-T_{90} period, T_{90} period, and Post-T_{90} period described in Section 3.2, the results of which are presented in Table 2.

For the T_{90} period, the BAND+BB model is not suitable to fit the gamma-ray data with an unconstrained β, e.g., $\beta < -5.0$. Note that the BIC value in the CPL+BB model is also smaller by 6.1 than that in the BAND+BB model. The CPL+BB model has a ΔBIC larger than two other models by 6, such as 7.5 with respect to the BAND model and 14.4 with respect to the CPL model, and thus is considered the best-fit model. The energy fluxes of the CPL component and the BB component in the CPL+BB model are calculated in the energy range between 8 keV and 40 MeV, such as an F_{CPL} and F_{BB} of $(8.7 \pm 1.8) \times 10^{-6}$erg cm^{-2} s^{-1} and $(1.2 \pm 0.5) \times 10^{-6}$erg cm^{-2} s^{-1} respectively. The BB component has about 12% of the total modeled energy flux. The νF_ν peak energy of the CPL component is 508 ± 65 keV while the BB component has a temperature of $kT_{BB} = 43 \pm 4$ keV. The νF_ν spectral energy distribution (SED) fitted by the CPL+BB model is plotted at the top right of Figure 2.

For the Pre-T_{90} period, one can see that the CPL model is suitable for fitting the gamma-ray spectrum with ΔBIC larger than 6 compared to the other three models, thus the CPL model is the best-fit model in the Pre-T_{90} period, which is plotted at the top left of Figure 2.

For the Post-T_{90} period, the parameters could not be constrained well in both BAND and BAND+BB models. The CPL model is the better model to fit the data compared with the CPL+BB model, i.e., ΔBIC = 6.1. Therefore, the best-fit model for the Post-T_{90} period is the CPL model, which is plotted at the bottom of Figure 2.

3.3.3. Time-resolved Spectral Analysis

Time-resolved spectral analysis of GRB 170206A in six epochs is performed, such as [T_0+0.208 s, T_0+0.394 s] for epoch a, [T_0+0.394 s, T_0+0.650 s] for epoch b, [T_0+0.650 s, T_0+0.782 s] for epoch c, [T_0+0.782 s, T_0+1.138 s] for epoch d, [T_0+1.138 s, T_0+1.221 s] for epoch e, and [T_0+1.221 s, T_0+1.376 s] for epoch f. In these spectral fittings, we set the initial spectral parameter values to be the same as the resultant parameter values from spectral analysis in the GBM T_{90} period.

First, as seen in Table 2, the time-resolved spectra in all epochs are not well fitted by the BAND+BB model due to the unconstrained high-energy photon index β except for epoch d. Even in epoch d, the BIC value derived by the model BAND +BB is larger by 9.9 than that derived by the models of CPL, indicating a worse fit. Note that the BIC of the BAND+BB model in each epoch is larger by 6 than that of the model with the minimum BIC. . Therefore, the BAND+BB model is rejected to fit the time-resolved gamma-ray spectra of GRB 170206A.

Second, we compare the BAND model and CPL model. With respect to the CPL model, the BAND model has a ΔBIC of 6.2, 6.1, and 6.0 in epochs a, e, and f respectively, which implies that the CPL model is the better model. In the other three epochs (b, c, and d), the CPL model in each epoch has a smaller BIC value than the BAND model; however, the ΔBIC is less than 6, such as 3.7, 3.2, and 4.3, respectively. With a minimum BIC in each epoch, we thus preferred the CPL model as a good model to fit all time-resolved spectra.

Finally, when comparing the CPL model and the CPL+BB model, the CPL+BB model is a better model to fit the spectrum than the CPL model in epoch b with ΔBIC = 11.1. The CPL model is a better model to fit the spectra in epoch a (ΔBIC = 9.6) and epoch f (ΔBIC = 11.2). For epochs c and d, the CPL has smaller BIC values but with the ΔBIC smaller than 6, such as 5.5 and 4.3, respectively; therefore, we cannot reject the CPL+BB model in these two epochs. For epoch e, the CPL+BB model has a smaller BIC than the CPL model, i.e., ΔBIC is 1.0, thus the CPL model is a comparable model in this epoch.

In total, the CPL+BB model is the best-fit model in epoch b and could be a comparable model in epochs c, d, and e. The CPL model is the best-fit model in epochs a and f and could be a comparable model in epochs c, d, and e.

In order to discuss the parameter and flux variations during the GBM T_{90}, we, therefore, select the CPL+BB model as the fitting model in the following analysis except for epoch a, and all $\nu F\nu$ SEDs are plotted in Figure 3. Note that, for epoch a, the α_{CPL} in the CPL+BB model is very hard, such as +2.25 (±0.72), thus we finally prefer the CPL model for epoch a.

In Figure 4, temporal variations of the resultant parameters are plotted as well as the multiwavelength GBM light curves. In the panel of the CPL index (α_{CPL}), the low-energy photon indices of epochs a, b, c, d, and e are all outside the synchrotron limit (–2/3), which implies that the CPL component could not be of standard synchrotron origin. For other epochs, such as Pre-T_{90}, f, and Post-T_{90}, α_{CPL} is also located more or less around the boundary of the synchrotron limit.

For the peak energy of the CPL component ($E_{p,\,CPL}$) and the temperature of the BB component (kT_{BB}), they track each other well, e.g., decaying–rising–decaying. The correlation is tested in the time-resolved spectra by employing the linear regression method in the *Origin* software package, which returns the Pearson correlation coefficient (R) and the chance probability of a null hypothesis (p). A strong positive correlation can be claimed when $R > 0.8$ while a moderate positive correlation can be claimed when $0.5 < R < 0.8$ (Newton & Rudestam 1999). We find that kT_{BB} is strongly positively correlated with $E_{p,\,CPL}$, with $R = 0.865$ and $p = 0.026$, as

$$E_{p,CPL} = 10^{1.20\pm0.42} kT_{BB}^{0.95\pm0.28}, \quad (4)$$

as seen in Figure 5, where both $E_{p,CPL}$ and kT_{BB} are in units of keV.

For the energy fluxes in time-resolved epochs derived from the CPL+BB model, the CPL fluxes (F_{CPL}) also track the BB fluxes (F_{BB}) well. The correlation analysis between them also

Table 2
Spectral-fitting Results of GRB 170206A

Models	Main Component				BB Component		Stat. and dof	
	BAND or CPL				BB			
$T_{\rm Start}-T_{\rm End}$ s − s	$E_{\rm p,\ main}$ keV	α	β	$F_{\rm main}$ 10^{-6}erg cm^{-2} s^{-1}	$kT_{\rm BB}$ keV	$F_{\rm BB}$ 10^{-6}erg cm^{-2} s^{-1}	AIC/BIC/-log (likelihood)	dof
Time-integrated								
Pre-T_{90}								
−0.133–0.208								
BAND	382 ± 79	−0.91 ± 0.11	<−5	2.0 ± 1.7	⋯	⋯	818.3/834.9/405.1	474
BAND+BB	10 ± 10	−1.02 ± 0.21	−1.66 ± 0.08	0.7 ± 0.4	58 ± 7	2.1 ± 0.10.5	836.7/861.6/412.3	472
CPL	380 ± 116	−0.91 ± 0.12	⋯	1.9 ± 1.3	⋯	⋯	816.3/828.8/405.1	475
CPL+BB	328 ± 136	−0.35 ± 0.46	⋯	1.6 ± 0.7	9 ± 2	<0.01	816.8/837.6/403.4	473
T_{90}								
0.208–1.376								
BAND	344 ± 14	−0.31 ± 0.04	−2.86 ± 0.17	10.8 ± 1.0	⋯	⋯	3038.9/3055.5/1515.4	474
BAND+BB	508 ± 41	−0.58 ± 0.06	<−5	8.9 ± 1.4	43 ± 4	1.2 ± 0.4	3029.1/3054.1/1508.6	472
CPL	379 ± 17	−0.39 ± 0.03	⋯	9.1 ± 0.8	⋯	⋯	3049.9/3062.4/1521.9	475
CPL+BB	508 ± 65	−0.58 ± 0.07	⋯	8.7 ± 1.8	43 ± 4	1.2 ± 0.5	3027.1/3048.0/1508.6	473
Post-T_{90}								
1.376–1.497								
BAND	⋯	⋯	⋯	⋯	⋯	⋯	Unconstrained	474
BAND+BB	⋯	⋯	⋯	⋯	⋯	⋯	Unconstrained	472
CPL	85 ± 33	−0.43 ± 0.38	⋯	0.9 ± 0.4	⋯	⋯	−624.7/−612.2/−315.4	475
CPL+BB	168 ± 277	0.27 ± 3.35	⋯	2.7 ± 0.01	11 ± 2	0.4 ± 0.1	−626.8/−606.1/−318.5	473
Time-resolved								
(a) 0.208–0.394								
BAND	345 ± 30	−0.16 ± 0.13	−5.80 ± 2.74	4.7 ± 1.0	⋯	⋯	190.6/207.3/91.3	474
BAND+BB	359 ± 29	2.29 ± 1.85	<−5	3.9 ± 2.2	24 ± 5	0.6 ± 0.4	191.9/216.9/90.0	472
CPL	345 ± 53	−0.16 ± 0.14	⋯	4.3 ± 1.2	⋯	⋯	188.6/201.1/91.3	475
CPL+BB	359 ± 63	2.25 ± 0.72	⋯	3.4 ± 2.2	24 ± 3	0.8 ± 0.3	189.9/210.7/90.0	473
(b) 0.394–0.650								
BAND	479 ± 39	−0.22 ± 0.07	−2.95 ± 0.40	19.4 ± 3.8	⋯	⋯	937.0/953.7/464.5	474
BAND+BB	804 ± 93	−0.53 ± 0.08	<−5	16.4 ± 3.6	57 ± 5	2.8 ± 1.1	920.0/945.1/454.0	472
CPL	529 ± 42	−0.30 ± 0.05	⋯	16.6 ± 2.4	⋯	⋯	937.5/950.0/465.8	475
CPL+BB	804 ± 136	−0.53 ± 0.08	⋯	15.6 ± 4.0	57 ± 5	2.8 ± 1.1	918.0/938.9/454.0	473
(c) 0.650–0.782								
BAND	331 ± 24	−0.02 ± 0.10	−2.96 ± 0.40	17.9 ± 3.9	⋯	⋯	−23.3/−6.6/−15.6	474
BAND+BB	471 ± 1	−0.33 ± 0.06	<−5	13.1 ± 1.0	50 ± 1	2.7 ± 0.6	−22.7/2.3/−17.4	472
CPL	362 ± 31	−0.11 ± 0.08	⋯	14.8 ± 2.6	⋯	⋯	−22.4/−9.8/−14.2	475
CPL+BB	470 ± 113	−0.33 ± 0.17	⋯	13.1 ± 5.4	50 ± 8	2.6 ± 1.6	−24.7/−4.3/−17.4	473
(d) 0.782–1.138								
BAND	200 ± 18	−0.20 ± 0.11	−3.04 ± 0.61	6.0 ± 1.6	⋯	⋯	1163.5/1180.1/577.7	474
BAND+BB	245 ± 20	−0.17 ± 0.20	−4.03 ± 1.31	5.0 ± 1.4	20 ± 4	0.4 ± 0.3	1160.6/1185.6/574.3	472
CPL	214 ± 16	−0.26 ± 0.07	⋯	4.9 ± 0.7	⋯	⋯	1163.3/1175.8/578.6	475
CPL+BB	246 ± 40	−0.17 ± 0.20	⋯	4.6 ± 1.6	19 ± 4	0.4 ± 0.3	1159.3/1180.1/574.6	473
(e) 1.138–1.221								
BAND	541 ± 43	−0.33 ± 0.08	−5.41 ± 2.52	19.8 ± 3.1	⋯	⋯	−593.2/−576.5/−300.6	474
BAND+BB	693 ± 86	−0.21 ± 0.19	<−10	17.6 ± 5.2	35 ± 6	1.7 ± 1.1	−602.4/−577.4/−307.2	472
CPL	542 ± 67	−0.33 ± 0.08	⋯	18.7 ± 3.7	⋯	⋯	−595.2/−582.6/−300.6	475
CPL+BB	693 ± 141	−0.21 ± 0.20	⋯	17.8 ± 6.9	35 ± 6	1.7 ± 1.2	−604.4/−583.6/−307.2	473
(f) 1.221–1.376								
BAND	205 ± 25	−0.67 ± 0.12	−3.61 ± 1.58	3.4 ± 0.9	⋯	⋯	−136.6/−119.9/−72.3	474
BAND+BB	253 ± 67	−0.78 ± 0.23	<−10	2.9 ± 1.5	22 ± 9	0.1 ± 0.1	−133.5/−108.5/−72.8	472
CPL	210 ± 41	−0.68 ± 0.12	⋯	3.1 ± 0.9	⋯	⋯	−138.4/−125.9/−72.2	475
CPL+BB	253 ± 112	−0.79 ± 0.24	⋯	3.0 ± 1.5	22 ± 9	0.2 ± 0.1	−135.5/−114.7/−72.8	473

favors a strong positive correlation, such as

$$F_{\rm CPL,-6} = 10^{0.88\pm0.08} F_{\rm BB,-6}^{0.67\pm0.18}, \quad (5)$$

with $R = 0.884$ and $p = 0.019$, which can be seen in Figure 5. Here, $F_{-6} = 10^{-6}F$ and both fluxes are in units of erg cm^{-2} s^{-1}.

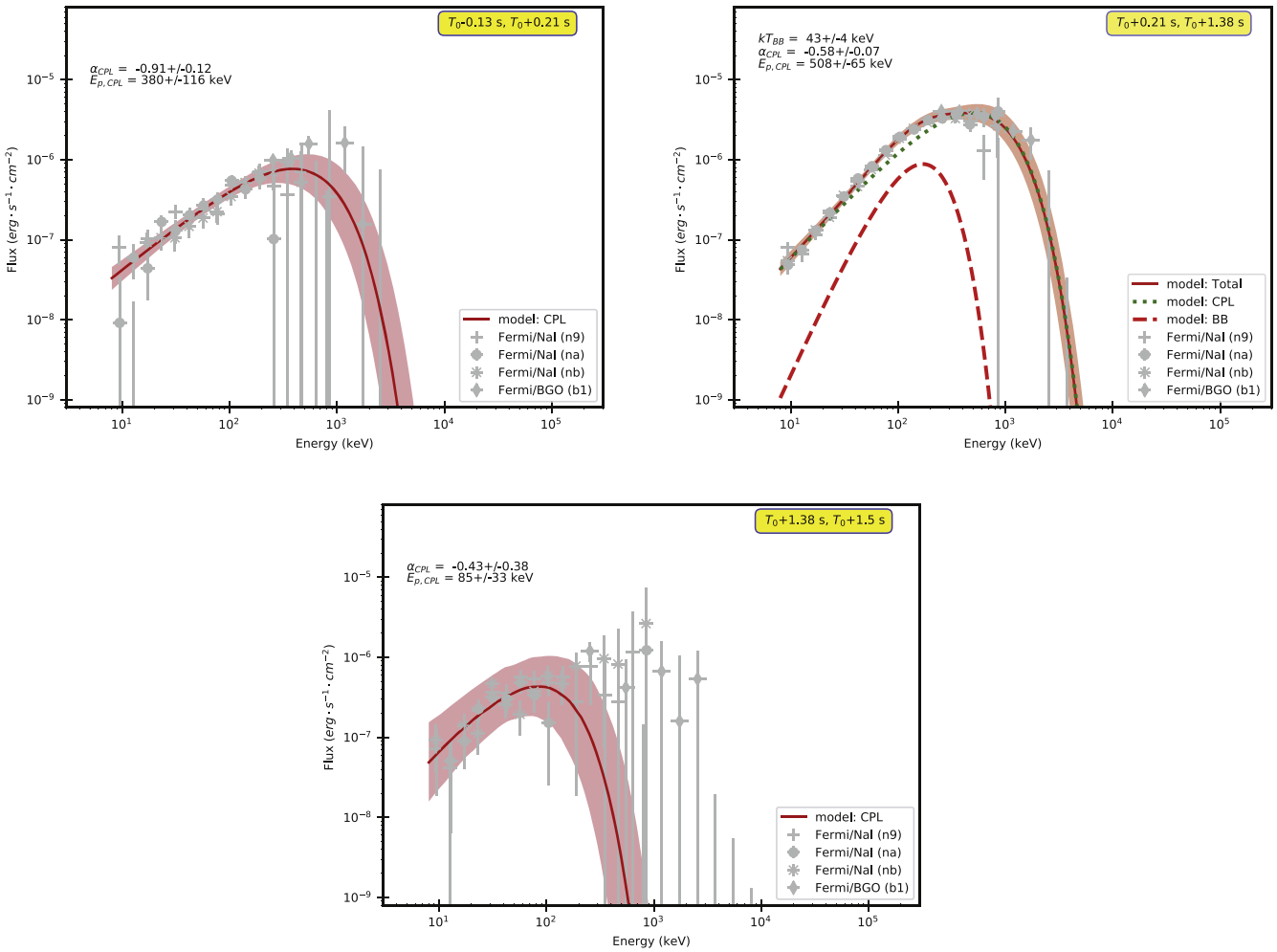

Figure 2. Spectral energy distributions and best-fitted model for the time-integrated spectra of GRB 170206A. Top left: Pre-T_{90} period between T_0-0.13 s and T_0+0.21 s. Top right: T_{90} period between T_0+0.21 s and T_0+1.38 s. Bottom: Post-T_{90} period between T_0+1.38 s and T_0+1.50 s. Data points are from the Fermi/GBM. For spectra best fitted by the CPL model, the red solid line represents the resultant CPL model. For spectra best fitted by the CPL+BB model, the green dotted line represents the CPL component, the red dashed line represents the BB component, and the red solid line is the total modeled flux. All red shaded regions are the 95% confidence intervals of the total modeled flux.

4. Origin of Thermal and Nonthermal Components and Its Implications

In addition to the four adopted spectral models in Table 2, i.e., BAND, BAND+BB, CPL, and CPL+BB, we have compared other spectral models in Appendix as well. As we can see, the other models do not present distinct advantages, so next, we focus on the four popular spectral models shown in Table 2 to explore their possible physical origins. Table 2 shows the fitting parameters of the spectra for the models of BAND, BAND+BB, CPL, and CPL+BB. When the BAND function is involved, either for the single BAND model or the BAND+BB model, usually, a very steep photon index at the higher energy band, namely, a very small β, has to be invoked. Such a small value of β makes the BAND function approach the spectral shape of the CPL, implying that the real spectral shape may follow the CPL function rather than the typical BAND function. In addition, for the time-integrated and time-resolved spectra in most cases during T_{90} (see Section 3.3), one can see the CPL+BB model fits better compared with the single CPL model. Although in some cases a single CPL model is good enough, this may be caused by the different weights of two components (BB and CPL components), inducing one component that is overshot by the other one. As a result, we take a more complicated observed spectral shape that contains two parts, i.e., a thermal component (the BB component) and a nonthermal component (the CPL component), to study their possible origins.

Besides, from the third and fourth panels of Figure 4, one can see the plausible common evolution between the BB component and the CPL component, indicating a correlation between both components. Figure 5 shows their correlations, as seen in Equations (4) and (5), which are stated as $E_{\rm p,CPL} \propto kT_{\rm BB}^{0.95\pm0.28}$ and $F_{\rm CPL} \propto F_{\rm BB}^{0.67\pm0.18}$.

Based on the above analyses, we suggest that the thermal emission and the nonthermal emission could imply two radiation regions (Mészáros et al. 2002). Basically, the thermal emission is a natural prediction from the photosphere of "fireball" model (Mészáros & Rees 2000; Mészáros et al. 2002; Rees & Mészáros 2005). Usually, the photons are coupled with the outflow due to the large optical depth at small radii, and the spectrum emerging at the photosphere is shown as the blackbody distribution. Apart from this thermal emission from the photospheric origin, the nonthermal part could originate from the energy dissipation above the photosphere. Electrons above the photosphere could be accelerated to a nonthermal

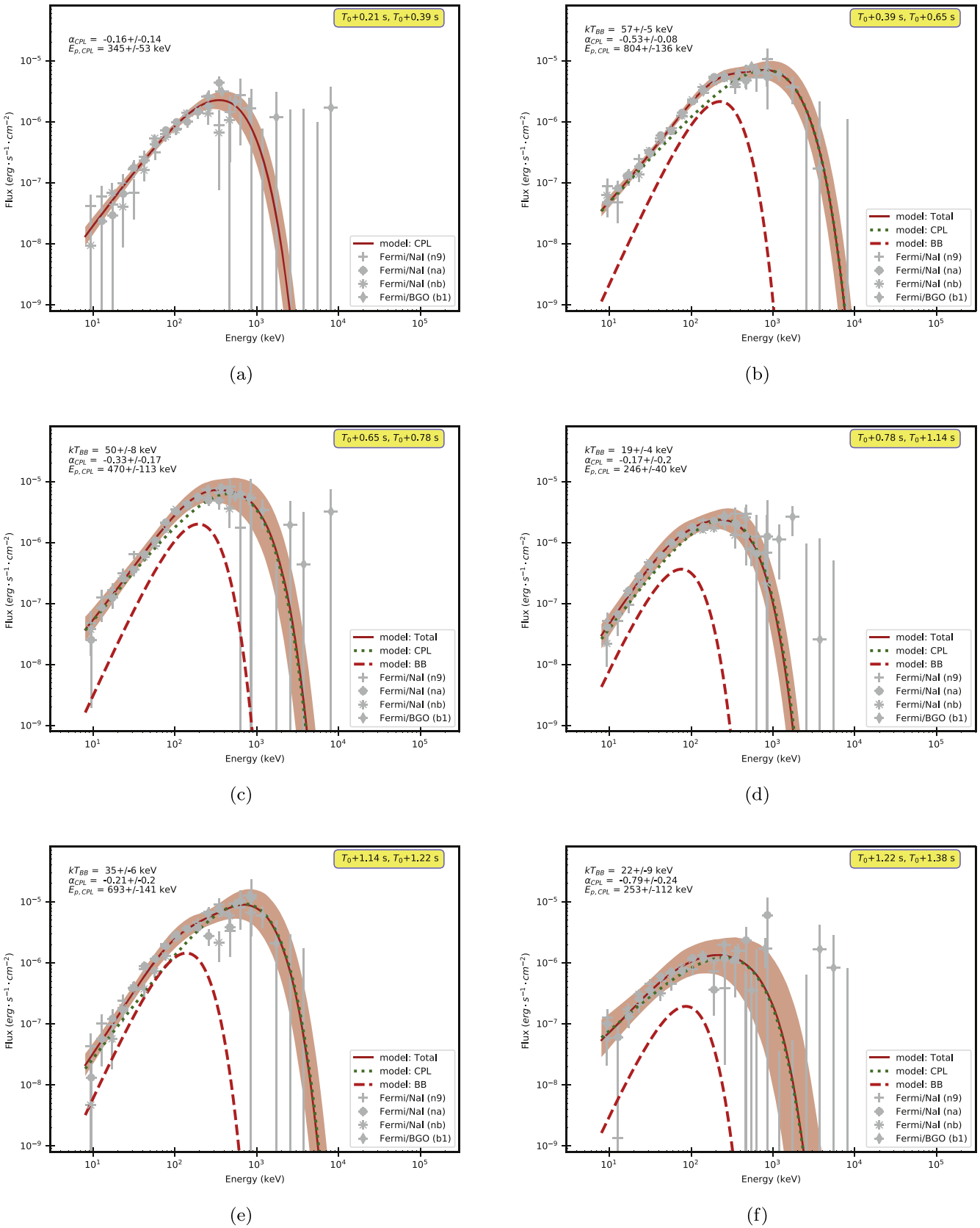

Figure 3. Same as Figure 2, but for the time-resolved spectra of GRB 170206A during GBM T_{90}.

distribution. Thermal photons could serve as seed photons to Compton scattering of accelerated nonthermal energetic electrons above the photosphere and diverse setups of thermal photons could affect the final nonthermal spectrum emitted by these electrons (Pe'er et al. 2005, 2006, 2012; Samuelsson et al. 2022). In other words, the Comptonization of thermal photons

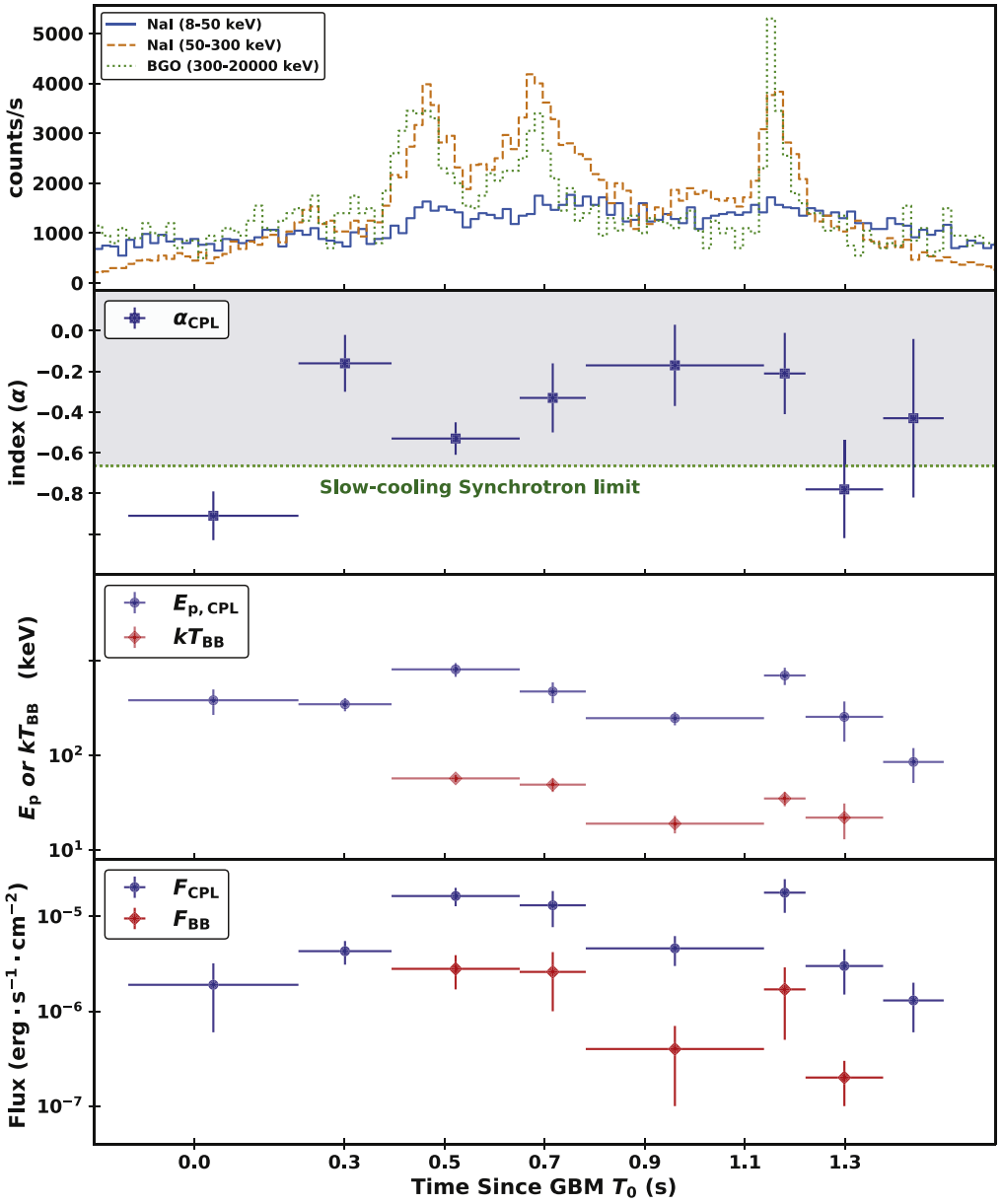

Figure 4. Parameter value distributions as a function of time. Top panel: count-rates lightcurves for three energy bands. Second panel: the low-energy photon index; the gray shadow is the prohibited region of the synchrotron process. Third panel: the peak energy ($E_{\rm p,\ CPL}$) in the νF_ν spectrum of the CPL component and the temperature of the BB component ($kT_{\rm BB}$). Bottom panel: the energy fluxes for the BB and CPL components.

shows as an additional nonthermal component to the thermal component. Such a connection between the thermal emission and the nonthermal emission may be responsible for the correlation between the BB component and the CPL component as shown in the third and fourth panels of Figure 4. Moreover, the low-energy spectral index of Comptonized photons, i.e., α, could be harder than the death line of synchrotron radiation (–2/3), inducing α ranging from -1.0 to 0.5 in some physical conditions (Deng & Zhang 2014). Such a range of α values is consistent with the low-energy photon indices listed in Table 2, especially for those indices that are significantly larger than $-2/3$.

Notice that the above suggested physical origin is based on the most preferred spectral functions, i.e., CPL or CPL+BB. The strong correlation between the BB component and the CPL component may be responsible for a single spectral function rather than two spectral functions, such as the mBB function mentioned in the Appendix although it has a worse BIC value. In this situation, the suggested radiation model above will be invalid and the actual physical origin could be totally different (Ahlgren et al. 2015; Vianello et al. 2018; Samuelsson et al. 2022).

5. Conclusion

In this work, we performed a comprehensive analysis of GRB 170206A with the observations by Fermi/GBM and Fermi/LAT in the prompt phase. A fast-variable thermal component is discovered, which has correlated photon fluxes with the nonthermal component throughout T_{90}. Hard low-energy photon indices (α) are found both in the time-integrated spectra and the time-resolved spectra. In the time-resolved spectra, the photon indices range from -0.79 to -0.16, most of which violate the line of death ($-2/3$) of the synchrotron slow-

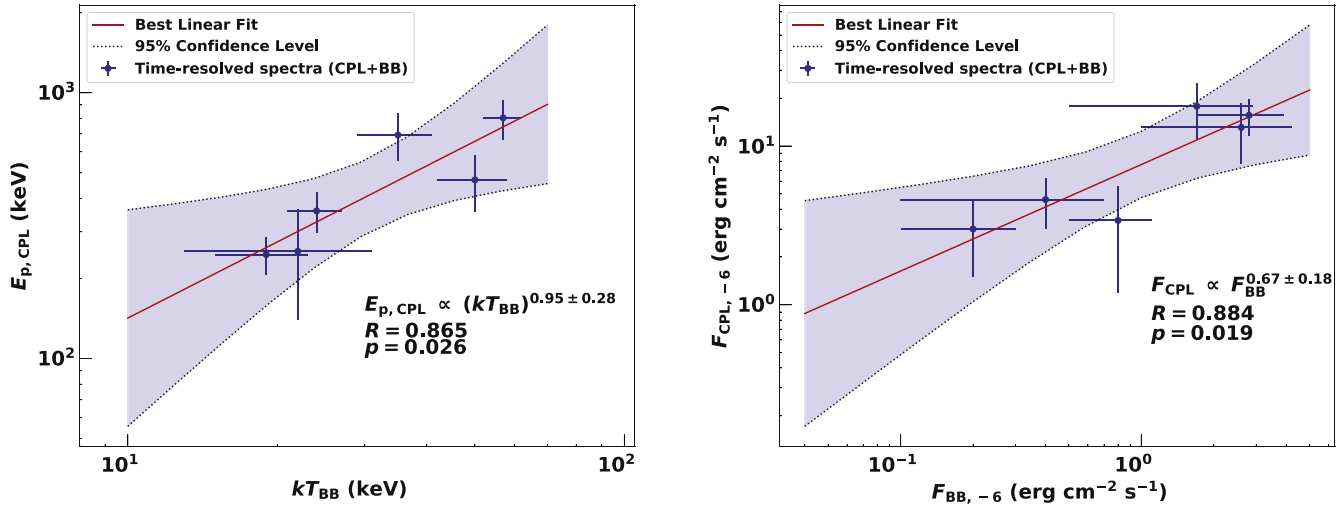

Figure 5. Correlations between the time-resolved spectral parameters among the GBM T_{90} of GRB 170206A when fitted by the CPL+BB model. Left: kT_{BB} vs. $E_{p,CPL}$. Right: $F_{BB,-6}$ vs. $F_{CPL,-6}$. The red lines are the best linear fitting, and the shadows are the 95% confidence levels of the best linear fitting. For each correlation, R is the Pearson correlation coefficient and p is the chance probability of the null hypothesis.

cooling radiation. In addition, we found the common evolution between the thermal component and the nonthermal component, indicating a positive correlation between photon fluxes as well as peak energies of both components. Based on the observational features, we explored the possible radiation models of GRB 170206A.

Assuming the two radiation regions for these two spectral components, the thermal component comes from the photosphere and the nonthermal component is from the Comptonization of the thermal component by the accelerated nonthermal energetic electrons above the photosphere. Because thermal photons serve as seed photons for the Compton scattering of energetic electrons above the photosphere and thus affect the final nonthermal spectrum emitted by these electrons, the observational hard low-energy photon indices, as well as the positive correlation between their photon fluxes, can be reproduced.

We thank the anonymous referee for the constructive suggestions. We appreciate Francesco Capozzi and Ng Chun-Yu for improving the manuscript. This research made use of the High Energy Astrophysics Science Archive Research Center (HEASARC) Online Service at the NASA/Goddard Space Flight Center (GSFC). This work is supported by the NSFC under grants 11903017, 12065017, 11975116, and 12003007, the science research grants from the China Manned Space Project with No. CMS-CSST-2021-B11, Jiangxi Provincial Natural Science Foundation under grant 20212BAB201029, and the Fundamental Research Funds for the Central Universities (No. 2020kfyXJJS039).

Facilities: Fermi (GBM), Fermi (LAT).

Software: 3ML (Vianello et al. 2015).

Appendix
Comparisons of 10 Spectral Models of GRB 170206A

By including 6 more spectral models, there are 10 spectral models are employed to fit the time-integrated and time-resolved SEDs of GRB 170206A and are selected to make comparisons. For example, the mBB, a single standard blackbody model (BB), double BB model (BB+BB), BB plus an additional power-law decay model (BB+PL), BAND with an additional PL model (BAND+PL), and CPL with an additional PL model (CPL+PL). For the mBB model, the same photon spectral function is employed as that in Iyyani & Sharma (2021), that is, the model named diskpbb in Xspec, which can be written as

$$N(E)_{\rm mBB} = \frac{4\pi E^2}{h^2c^2}\left(\frac{A_{\rm mBB}}{\zeta}\right)T_p^{(2/\zeta)}\int_{T_{\rm min}}^{T_p}\frac{T^{\frac{-(2+\zeta)}{\zeta}}}{e^{(E/T)}-1}dT, \quad \text{(A1)}$$

where $A_{\rm mBB}$ is the amplitude, ζ is the power-law index of the radial dependence of the temperature ($T(r)\propto r^{-\zeta}$), T_p is the peak temperature in keV, and $T_{\rm min}$ is the minimum temperature of the underlying blackbodies and is considered to be well below the energy range of the observed data, i.e., 8 keV in this work. For the PL function above, its photon model is presented as

$$N(E)_{\rm PL} = A_{\rm PL}\left(\frac{E}{100\ {\rm keV}}\right)^{\Gamma}, \quad \text{(A2)}$$

where $A_{\rm PL}$ is the amplitude, and Γ is the power-law spectral index.

As seen in Table. A1, there are three candidate models with ΔBIC close to 0, that is, mBB, CPL, and CPL+BB. For the Pre-T_{90} and Post-T_{90} periods, the CPL and the mBB models are the compared models. However, in the T_{90} period, the CPL +BB model is the unique best model to fit its SED, which has none compared models. In the time-resolved spectra, the CPL model is the compared/best model in epochs a, c, d, e, and f, the mBB model is the compared/best model in epochs a, c, and f. The CPL+BB model is the compared/best model in epochs b, c, d, and e.

We did not present the result of the mBB model in the main text for two reasons. On the one hand, the mBB model is ruled out in the T_{90} period and three epochs (b, d, and e), which include two intensive main pulses, such as P1 and P3. On the other hand, the CPL model usually has a smaller BIC than the mBB model, such as in epochs c and f; even in epoch a, the mBB model has a BIC only 0.1 smaller than that in the CPL model. Therefore, we did not present the details of the mBB model in the main text. Although the BAND or BAND+BB

Table A1
ΔBIC between Each Candidate Model and the Model with the Minimum BIC[a]

Period	BAND	BAND+BB	BAND+PL	CPL	CPL+BB	CPL+PL	BB	BB+BB	BB+PL	mBB
Post-T_{90}	Unconstrained	Unconstrained	Unconstrained	0	6.1	Unconstrained	10.0	22.3	5.5	1.7
Pre-T_{90}	6.5	33.1	34.2	0.3	9.1	Unconstrained	101.5	113.8	20.8	0
T_{90}	7.6	6.2	339.7	14.4	0	26.7	1327.3	182.7	374.5	44.8
a	6.3	15.9	39.6	0.1	9.7	Unconstrained	51.2	3.6	23.0	0
b	14.8	6.2	143.0	11.1	0	23.5	385.5	63.6	138.5	22.0
c	3.2	12.1	108.7	0	5.5	11.6	178.1	26.4	52.2	3.9
d	4.4	9.9	Unconstrained	0	4.4	11.4	285.0	9.1	76.0	6.5
e	7.1	6.2	68.9	0.9	0	13.3	183.6	1.1	101.2	6.8
f	6.0	17.4	Unconstrained	0	11.2	8.1	112.6	14.1	20.7	2.2

Note.
[a] The ΔBIC of the model with the minimum BIC is presented as 0.

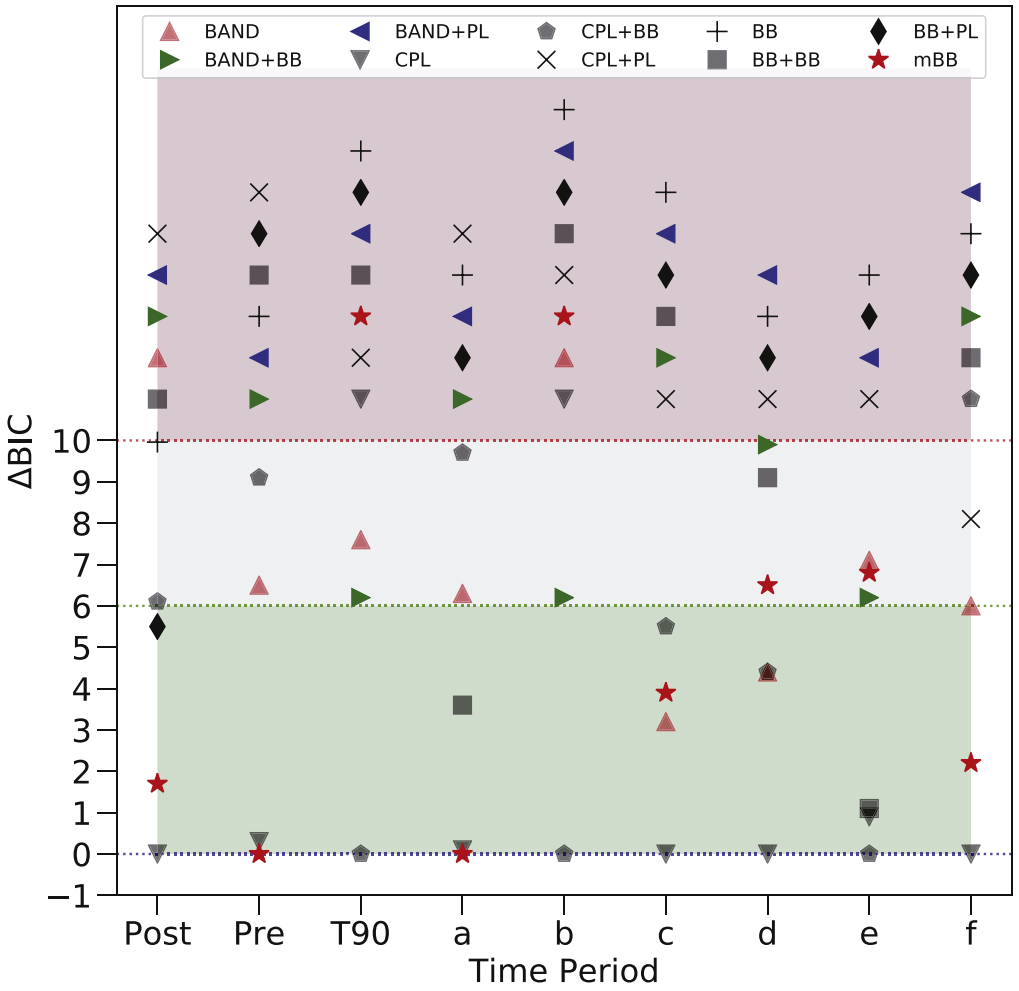

Figure 6. ΔBIC between each candidate model and the model with minimum BIC. Post-, Pre-, and T_{90} represent the time-integrated spectra in Post-T_{90}, Pre-T_{90}, and T_{90} periods. The labels a to e are the time-resolved spectra in six epochs between the GBM T_{90} duration. For three shadow regions, models in the dark red region (top) have ΔBIC larger than 10, thus all candidate models are rejected with very strong evidence; for models in the dark gray region (middle, $6 < \Delta\mathrm{BIC} < 10$), the candidate models are not recommended with strong evidence; models in the dark green region (bottom, $\Delta\mathrm{BIC} < 6$) are the compared models with respect to the model with the minimum BIC.

model has a ΔBIC that is mostly larger than 6 as seen in Figure 6, we include them in the main text because they are the popular models being considered in many published papers.

ORCID iDs

Qing-Wen Tang https://orcid.org/0000-0001-7471-8451
Yuan-Chuan Zou https://orcid.org/0000-0002-5400-3261

References

Ackermann, M., Ajello, M., Asano, K., et al. 2013, ApJS, 209, 11
Acuner, Z., Ryde, F., & Yu, H.-F. 2019, MNRAS, 487, 5508
Acuner, Z., Ryde, F., Pe'er, A., et al. 2020, ApJ, 893, 128

Ajello, M., Arimoto, M., Axelsson, M., et al. 2019, ApJ, 878, 52
Ahlgren, B., Larsson, J., Nymark, T., Ryde, F., & Pe'er, A. 2015, MNRAS, 454, L31
Akaike, H. 1974, ITAC, 19, 716
Axelsson, M., Baldini, L., Barbiellini, G., et al. 2012, ApJL, 757, L31
Band, D., Matteson, J., Ford, L., et al. 1993, ApJ, 413, 281
Battelino, M., Ryde, F., Omodei, N., et al. 2007, in AIP Conf. Proc. 921, The First GLAST Symposium, 921 (Melville, NY: AIP), 478
Beloborodov, A. M. 2010, MNRAS, 407, 1033
Beloborodov, A. M. 2011, ApJ, 737, 68
Burgess, J. M., Ryde, F., & Yu, H.-F. 2015, MNRAS, 451, 1511
Burns, E., Veres, P., Connaughton, V., et al. 2018, ApJL, 863, L34
Cash, W. 1979, ApJ, 228, 939
Daigne, F., Bošnjak, Ž, & Dubus, G. 2011, A&A, 526, A110
Deng, W., & Zhang, B. 2014, ApJ, 785, 112
Derishev, E. V., Kocharovsky, V. V., & Kocharovsky, V. V. 2001, A&A, 372, 1071
Dirirsa, F. F., Tak, D., Vianello, G., et al. 2017, GCN, 20617, 1
Fenimore, E. E., Klebesadel, R. W., Laros, J. G., et al. 1982, Natur, 297, 665
Ghirlanda, G., Ghisellini, G., Salvaterra, R., et al. 2013, MNRAS, 428, 1410
Giannios, D. 2012, MNRAS, 422, 3092
Goldstein, A., Burgess, J. M., Preece, R. D., et al. 2012, ApJS, 199, 19
Goodman, J. 1986, ApJL, 308, L47
Guiriec, S., Connaughton, V., Briggs, M. S., et al. 2011, ApJL, 727, L33
Guiriec, S., Daigne, F., Hascoët, R., et al. 2013, ApJ, 770, 32
Hurley, K., Mitrofanov, I. G., Golovin, D., et al. 2017, GCN, 20623, 1
Iyyani, S., Ryde, F., Axelsson, M., et al. 2013, MNRAS, 433, 2739
Iyyani, S., & Sharma, V. 2021, ApJS, 255, 25
Kaneko, Y., Preece, R. D., Briggs, M. S., et al. 2006, ApJS, 166, 298
Kass, R., & Raftery, A. 1995, J. Am. Stat. Assoc., 90, 773
Katz, J. I. 1994, ApJ, 422, 248
Larsson, J., Racusin, J. L., & Burgess, J. M. 2015, ApJL, 800, L34
Lundman, C., Pe'er, A., & Ryde, F. 2013, MNRAS, 428, 2430
Lundman, C., Pe'er, A., & Ryde, F. 2014, MNRAS, 440, 3292
Lundman, C., Vurm, I., & Beloborodov, A. M. 2018, ApJ, 856, 145
Matz, S. M., Forrest, D. J., Vestrand, W. T., et al. 1985, ApJL, 288, L37
Mazets, E. P., Golenetskii, S. V., Aptekar, R. L., et al. 1981, Natur, 290, 378
Mészáros, P., & Rees, M. J. 2000, ApJ, 530, 292
Mészáros, P., Ramirez-Ruiz, E., Rees, M. J., et al. 2002, ApJ, 578, 812
Nakar, E., Ando, S., & Sari, R. 2009, ApJ, 703, 675
Newton, R. R., & Rudestam, K. E. 1999, Your Statistical Consultant: Answers to your Data Analysis Questions (Thousand Oaks, CA: Sage Publications)
Paczynski, B. 1986, ApJL, 308, L43
Pe'er, A. 2008, ApJ, 682, 463
Pe'er, A., Mészáros, P., & Rees, M. J. 2005, ApJ, 635, 476
Pe'er, A., Mészáros, P., & Rees, M. J. 2006, ApJ, 642, 995
Pe'er, A., & Ryde, F. 2011, ApJ, 732, 49
Pe'er, A., & Zhang, B. 2006, ApJ, 653, 454
Pe'er, A., Zhang, B.-B., Ryde, F., et al. 2012, MNRAS, 420, 468
Preece, R., Burgess, J. M., von Kienlin, A., et al. 2014, Sci, 343, 51
Rees, M. J., & Meszaros, P. 1994, ApJL, 430, L93
Rees, M. J., & Mészáros, P. 2005, ApJ, 628, 847
Ryde, F. 2004, ApJ, 614, 827
Ryde, F. 2005, ApJL, 625, L95
Ryde, F., Lundman, C., & Acuner, Z. 2017, MNRAS, 472, 1897
Samuelsson, F., Lundman, C., & Ryde, F. 2022, ApJ, 925, 65
Sari, R., Narayan, R., & Piran, T. 1996, ApJ, 473, 204
Sari, R., Piran, T., & Narayan, R. 1998, ApJL, 497, L17
Scargle, J. D., Norris, J. P., Jackson, B., et al. 2013, ApJ, 764, 167
Schwarz, G. 1978, AnSta, 6, 461
Svinkin, D., Golenetskii, S., Aptekar, R., et al. 2017, GCN, 20625, 1
Tang, Q.-W., Wang, K., Li, L., et al. 2021, ApJ, 922, 255
Tavani, M. 1996, ApJ, 466, 768
Uhm, Z. L., & Zhang, B. 2014, NatPh, 10, 351
Veres, P., Zhang, B.-B., & Mészáros, P. 2012, ApJL, 761, L18
Vianello, G., Gill, R., Granot, J., et al. 2018, ApJ, 864, 163
Vianello, G., Lauer, R. J., Younk, P., et al. 2015, arXiv:1507.08343
von Kienlin, A., Meegan, C. A., Paciesas, W. S., et al. 2020, ApJ, 893, 46
von Kienlin, A., & Roberts, O. J. 2017, GCN, 20616, 1
Wang, K., & Dai, Z.-G. 2021, Galax, 9, 68
Wang, X.-Y., Li, Z., Dai, Z.-G., et al. 2009, ApJL, 698, L98
Wang, Y., Xiong, S., & Zhao, Y. 2017, GCN, 20624, 1
Zhang, B. 2020, NatAs, 4, 210
Zou, Y. C., Cheng, K. S., & Wang, F. Y. 2015, ApJL, 800, L23